



Deformation and fracture of aluminium foams under proportional and non proportional multi-axial loading: statistical analysis and size effect

J.-S. Blazy^{a,b,c}, A. Marie-Louise^a, S. Forest^{a,*}, Y. Chastel^b, A. Pineau^a, A. Awade^c,
C. Grolleron^c, F. Moussy^c

^aCentre des Matériaux P.-M. Fourt, Ecole des Mines de Paris, UMR CNRS 7633, BP 87, F-91003 Evry, France

^bCentre de Mise en Forme des Matériaux, Ecole des Mines de Paris, UMR CNRS 7635, 1 rue Claude Daunesse, F-06904 Sophia Antipolis, Cedex, France

^cRENAULT S.A. Direction de l'ingénierie des matériaux, Technocentre, TCR LAB 0 35, 1 av. du Golf, 78288 Guyancourt, Cedex, France

Received 12 August 2002; received in revised form 16 February 2004; accepted 8 March 2004

Abstract

An extensive experimental programme and detailed mechanical analysis were performed to test and model the statistical response of metallic foams under complex loading conditions. Tensile tests were performed on more than 80 specimens of closed-cell aluminium foams with four different specimen sizes. These test results show a large scatter and a significant size effect especially on standard deviation. The average fracture stress and, more significantly, the corresponding scatter decrease for increasing volume sizes. An attempt is made to use the Weibull statistical analysis to interpret these variations. A Weibull modulus close to 8 is found. Compression tests were also carried out. Both mean fracture stress in tension and mean peak stress in compression and the corresponding dispersions are correctly described by a single set of Weibull parameters. The statistical model is extended to multi-axial loading conditions by introducing an effective stress measure involving both the deviatoric part of the stress tensor and its trace. One additional parameter is identified using the average shear yield stress obtained from pure shear tests and torsion tests on solid bars. It is shown that the model is able to predict the dispersion found for the shear strength. Two types of combined tension/compression–torsion loading conditions were then tested experimentally. The non-proportional loading path consists of a tension test followed by torsion, keeping the axial stress constant. In the proportional loading path, shear and axial stress follow a straight line in the stress space. The corresponding surface of average yield/fracture stress is found to be symmetric. The experimental results are in good agreement with the predictions of the statistical model. The model predicts a bell-shaped surface for the first loading path and a quasi-elliptic one for the proportional one. The scatter found in the description of this surface is also

* Corresponding author. Tel.: +33-1-6076-3051; fax: +33-1-6076-3150.

E-mail address: samuel.forest@mat.ensmp.fr (S. Forest).

accounted for accurately by the model. A brief discussion of an extension of Beremin's micromechanical model to the statistical failure of brittle foams is presented.

© 2004 Elsevier Ltd. All rights reserved.

Keywords: Aluminium foam; Fracture; Constitutive behaviour; Probability and statistics; Mechanical testing

1. Introduction

Recently, processing techniques for aluminium foams have been improved. These materials are becoming available for use in applications such as lightweight energy absorption devices for automotive industry (see e.g. Refs. [1,2]). The mechanical properties of these foams are now well-understood and design tools are available to include these materials in structural components [3,4]. However, successful industrial applications require not only a precise assessment of their average properties under complex loading conditions, but also of the corresponding scatter usually associated with these properties. The experimental determination and the modelling of mean material response and its dispersion under uni- and multi-axial loading are the main objectives of the present work.

The compressive behaviour of aluminium foams has been the subject of thorough investigations because of their encouraging energy dissipation capability [5]. Foam crushing proceeds through the formation, multiplication and propagation of strain localisation bands throughout the specimen [6,7]. In tension, aluminium foams usually exhibit a brittle behaviour. Tensile loading is also important in practice because structures may be submitted to bending and the resulting brittle tensile behaviour is a severe limitation for further energy absorption. However, studies of the tensile behaviour of metal foams remain scarce (see e.g. Refs. [5,8]). They are usually limited to a small number of samples, which does not allow a precise statistical analysis of the brittle behaviour. Note also that the compressive deformation of aluminium foam is not a purely ductile process but, instead, fracture takes place very early inside localised bands [6]. In the present work, it is confirmed that the deformation and fracture behaviour of metallic foams is a combination of local brittle behaviour and plastic yielding effects. In the paper the distinction between yielding and fracture will not be made except otherwise stated.

Experimental data for the multi-axial yielding of metallic foams are also very limited. The main contributions can be found in Refs. [9–11]. Typically, axisymmetric tests are performed on open- and closed-cell aluminium foams under combined axial and radial compression, on the one hand, and for a variety of biaxial, shear and axisymmetric loadings, on the other hand. Because of experimental scatter, these studies show that it remains difficult to establish the shape of the yield surfaces, at least concerning the initial yield surface. These data were obtained mainly with a compressive regime (except in Refs. [12] for polymeric foam) and results for multi-axial situations with superimposed tensile axial stress are still scarce. In the present work, the case of combined tension/compression–torsion loading is addressed, which makes it possible to study the symmetry properties of the initial yield/fracture surface. In the tensile mode, linear fracture mechanical concepts have been applied to notched specimens or other foams structures [13].

The scatter in most of the measured properties can be associated with the inevitable presence of defects in aluminium foams due to the material processing itself, e.g. the strongly non-homogeneous distribution of cell sizes. The effect of geometrical defects on the elastic and plastic properties of foams has been described by several authors [8,14]. These authors report that the localised yielding is

believed to result from local inhomogeneities such as variations in density, cell shape, cell orientation and cell wall curvature. However, these authors did not relate the statistical distribution of defect size to the dispersion of the measured properties nor to a possible size effect which can be evidenced using specimens of different sizes. The size effects reported in literature are rather related to edge effects [15], to the notch sensitivity or to the influence of hole size in foam structures [16,17]. In Ref. [18], Huang and Gibson related the fracture toughness of brittle open-cell foam with the cell size and the Weibull modulus of cell wall material. In Ref. [5], McCullough et al. performed a Weibull analysis of their tensile and compression tests but did not investigate the corresponding expected size effects. In the present work, the problem of the yield strength in compression and failure strength in tension of foam specimens as a function of specimen volume is investigated.

Widespread applications for aluminium foams require a precise modelling of the scatter for both uni- and multi-axial loading conditions in order to design components with a given level of confidence. Constitutive models for aluminium foams valid for multi-axial loading are now available for the initial yield surface but also in some cases for the post-yield behaviour [3,7,11,19–22]. They are based on the mechanics of porous materials developed for instance for powder metallurgy applications [23]. However, these models are purely deterministic and cannot account for the systematic scatter observed for aluminium foams in spite of continuing process and metallurgy improvement. The statistical aspect must also be incorporated in the multi-axial model to allow reliability assessments for structural applications.

The paper is organised as follows. After this first introductory section, Section 2 describes the microstructure of the investigated foams and the experimental mechanical testing procedures. The results of tensile tests on more than 80 specimens of four different specimen sizes are reported in the third section. Compression, shear, torsion and combined tension/compression–torsion tests have been performed and are described also in Section 3. Section 4 provides a statistical model of the tensile and compression tests accounting for the observed size effects. The model is then extended to shear/torsion loading conditions, and finally used to predict the mean response and dispersion under multi-axial loading. The predictions are then compared with experimental results for two types of loading conditions. The non-proportional loading path corresponds to an initial tension or compression loading followed by a torsion loading, keeping the axial load constant. For the proportional loading path, torque and axial force are applied simultaneously and follow a straight line in the torque/force space. Finally a simple micromechanical model providing the fracture statistics of brittle foams from the knowledge of the cell size distribution is presented.

Regarding notation, the statistical mean value of a physical property Z is denoted by \bar{Z} and its variance by D_Z^2 . The standard deviation is then D_Z . In all figures, the chosen convention is that the plotted intervals of confidence are the interval $[\bar{Z} - D, \bar{Z} + D]$ for the investigated property Z . For a background on Weibull statistics, the reader is referred to a number of studies [24–26].

2. Experimental procedures

2.1. Material: composition and microstructure

Flat plates of stabilised aluminium foam of nominal density 0.26 g/cm^3 were supplied by Hydro Aluminium. The plates were of dimension $2500 \text{ mm} \times 700 \text{ mm} \times 90 \text{ mm}$. They consisted of two skins

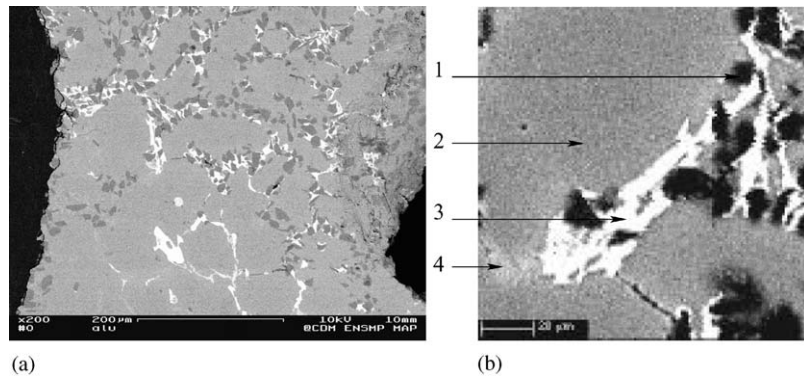


Fig. 1. (a) Cell wall microstructure (SEM micrograph), (b) Zoom on SiC particle (labelled 1) and the three main phases using microprobe analysis: matrix (labelled 2), Al–Si phase (labelled 3), intermetallic phase (labelled 4).

Table 1

Chemical composition of the three main phases of the aluminium alloy (wt%)

	Matrix	Al–Si phase	Intermetallic phase
Al	95.49	28.74	35.77
Si	0.66	61.99	19.98
Cu	2.09	5.89	10.89
Mg	0.41	0.64	3.28
Fe	0.43	0.25	18.29
Ni	0.03	0.02	0.81
C	0	0.96	0
O	0.92	1.49	1.06

with a foam core. As a result of the manufacturing process, the upper skin was thinner (0.5 mm approximately) than the lower one (1 mm). The global composition was: Si = 14.88, Fe = 2.82, Cu = 2.16, Ni = 0.6, Al = balance (in wt%).

In order to limit cell wall damage, each sample for microstructural observations was cut using electro-discharge machining. The specimens were infiltrated in vacuum by a low viscosity resin, as described in Ref. [27]. After being polished and nickel coated, the specimens were observed using a scanning electron microscope (SEM). The local composition was determined using energy dispersive X-ray spectroscopy (EDS). The SiC particules used in the process are retrieved and are labelled 1 in Fig. 1. The size of these particules is between 10 and 30 μm . They are preferentially found in the cell walls and are more seldom at the triple junctions. In addition to this network of SiC inclusions, three main phases were identified as shown in Fig. 1. The cell wall is made of an Al–Cu–Si–Mg phase (labelled 2 in Fig. 1), and an intermetallic phase Al–Ni–Fe–Si (labelled 3 in Fig. 1) and an Al–Si phase (labelled 4 in Fig. 1). The intermetallic phase is present in a secondary dendritic form, mainly at the triple junctions. The compositions of the three main phases are given in Table 1.

Three-dimensional X-ray tomography has been used to measure the distribution of cell size of aluminium foams (see e.g. Refs. [28,29]). This technique was applied by Benouali and Froyen

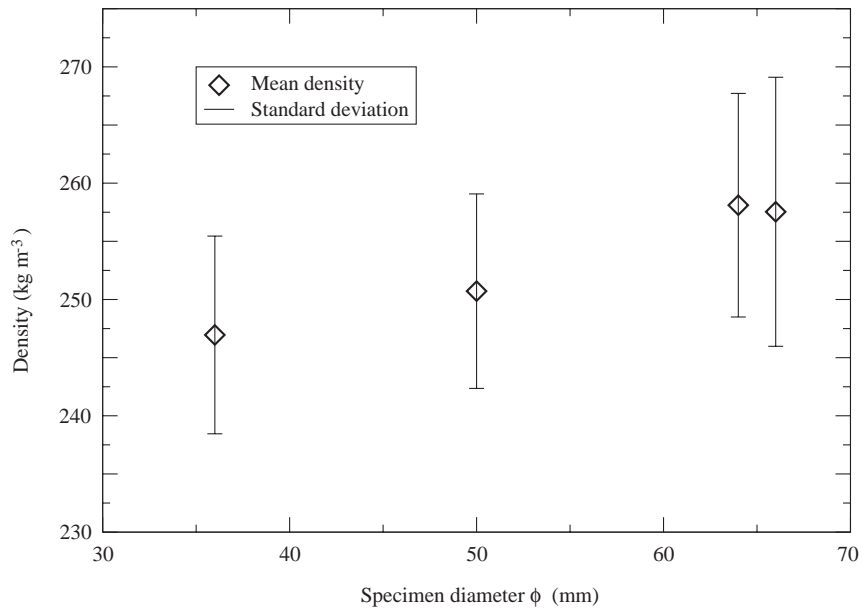


Fig. 2. Density variation of all tested specimens as a function of specimen diameter.

(KU Leuven) to our foam. The mean cell size was found to be 1.5 mm. The size of the biggest cells is about 9 mm. The size of the cell is defined as the diameter of a disk of the same area.

2.2. Mechanical testing

All foam specimens were characterised in terms of their density and visible cell morphology. Cube and cylinder specimens of different sizes were used. The density was measured using an electronic balance and measurement of dimensions using electronic calipers. The density varies from 245 to 260 kg/m³ (Fig. 2). The density of the samples extracted from the same foam plate exhibits a slight scatter. The dispersion depends on the location in the foam plate from which each specimen was extracted. Thus, for cylindrical specimens, the samples with the largest diameter (65 mm) display the highest density. This effect can be related to the density gradient from the skin to the core of the foam plate, as described in Ref. [30]. The largest cylindrical specimens called T1 and T2 in Table 2 (\varnothing 65 mm) are extracted closer to the skin region. This explains the slightly higher mean density of the larger specimens.

2.2.1. Compression tests

Cube specimens of dimensions 80 mm \times 80 mm \times 80 mm were sawn from the core of the foam plate in order to reduce the skin effect. The specimen were manufactured with special care in order to obtain the two opposite face as parallel as possible. The specimens were inserted between two parallel steel platens of a servo-hydraulic testing machine. The platens were lubricated with boron nitride-based spray. The tensile machine was equipped with a 100 kN load cell and the tests

Table 2

List of the different types of cylindrical tensile specimens investigated in this work

Sample	Number of samples	Length (mm)	Diameter (mm)	Volume (cm ³)
T1	27	180	65	$V_1 = 597$
T2	24	150	65	$V_2 = 497 \simeq V_1/1.2$
T3	21	150	50	$V_3 = 294 \simeq V_1/2$
T4	16	150	36	$V_4 = 152 \simeq V_1/4$

were carried out using displacement control with a cross-head speed of 0.5 mm s^{-1} . Three different directions with respect to the foam plate were tested in order to characterise the anisotropy.

2.2.2. Tensile tests

Tensile specimens were extracted from the flat plates along the longitudinal direction using a drilling machine. This machining device avoids geometrical fluctuations and gives a reference revolution surface. Then, each specimen is turned to machine both opposite faces. The result is a cylindrical specimen without major geometrical defect. Afterwards the specimen was glued to a fixing part which was then connected to the testing machine. The tensile apparatus consists of one ball-and-socket joint attached to a universal joint on each side of the fixing part (see Fig. 3a). Four specimen sizes, labelled T1–T4, were tested (cf. Table 2). The different volume sizes were determined in order to maximise the range between the biggest one T1 and the smallest one T4. For the biggest specimen the diameter of the cylinder is limited by the thickness of the foam plate and the length is limited by the ratio length on diameter to prevent instabilities during testing. For the smallest specimen, the volume was chosen in order to keep statistical representativity (see Ref. [31]). Uniaxial tension tests were carried out using an electro-mechanical tensile machine equipped with a load-cell of 50 kN. The tests were performed under displacement control with a cross-head speed of 0.1 mm s^{-1} .

2.2.3. Shear and torsion tests

Specimens of dimensions $250 \text{ mm} \times 25 \text{ mm} \times 50 \text{ mm}$ for the shear tests were cut from the foam plate in the longitudinal direction. The test is based on the European standard number ISO 1922–1981 (F) for organic materials. This test is comparable to the ASTM C-273 test method recommended in Ref. [4]. The sample was glued to two fixing devices attached to a tensile machine (see Fig. 3c). The shear load is applied by the longitudinal displacement of two stainless-steel plates. Because of the low force level, we assume that the two plates remain parallel during the test. This hypothesis is supported by FE computations.

In addition to these shear tests, torsion tests were carried out on cylindrical T2 specimens identical to those used for tensile tests. The fixing device is different since it must provide alignment between the sample and the tension–torsion machine axis and allow torque and axial force transmission (see Fig. 3b). The alignment between the sample and the machine's axis is checked using two dial gauges with a tolerance of 0.1 mm. The torsion tests were performed using a tension–torsion machine equipped with a 50 kN load-cell and a 1.2 kN m torque-cell. The tests were conducted using angle control with an angular speed of 0.1° s^{-1} .

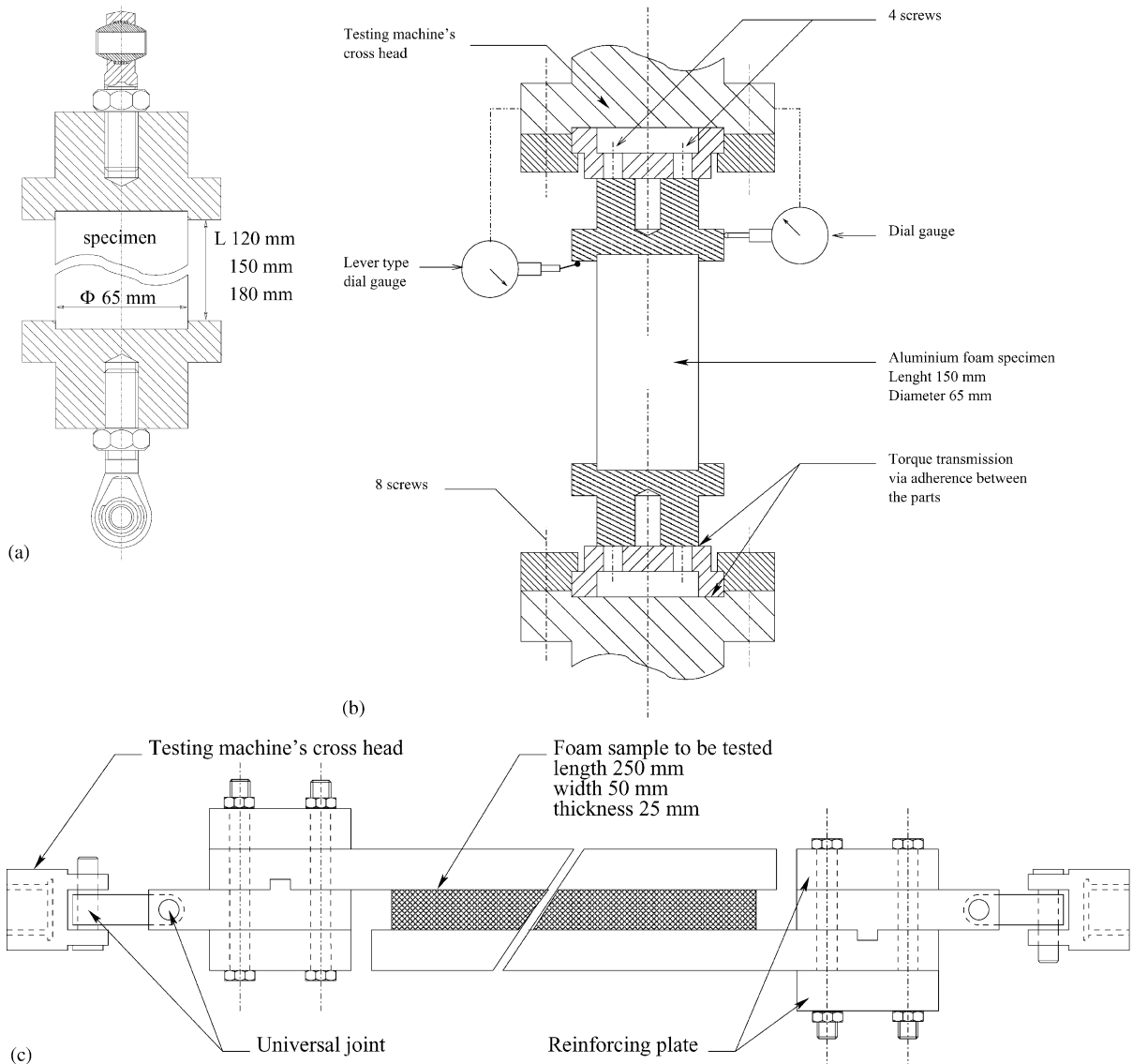


Fig. 3. Experimental apparatus: (a) specimen assembly and tensile setup, (b) modification of the tensile setup to perform tension–compression/torsion tests, (c) simple shear test setup.

2.2.4. Combined tension/compression–torsion tests

For these biaxial tests, the same T2-type specimens as those used for the tensile and torsion tests were tested. The fixing device and the tension–torsion machine were the same as those used for the torsion test. According to the type of loading path, the test can be performed using axial force control, torque control or both. Two types of loading paths were investigated (see Fig. 4): a non-proportional loading path (labelled 1 in Fig. 4) with axial force control and a proportional loading path (labelled

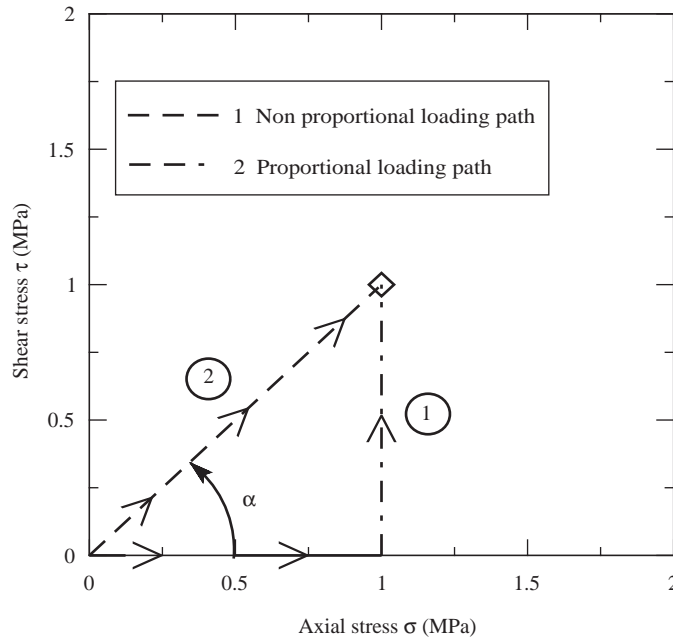


Fig. 4. Investigated loading paths for tension/torsion tests: non-proportional loading (number 1, tension followed by torsion), proportional loading (number 2).

2 in Fig. 4) with axial force control and torque control. For the non-proportional loading tests, axial force is prescribed first up to a given force and then an increasing torsion angle is applied, keeping the axial force constant. For the proportional tests, tension or compression and torsion are applied simultaneously and follow a straight line with a given slope in the torque/force space.

3. Experimental results

The detailed results for all tests are reported in Table 3. The main features for each type of test are described below.

3.1. Uni-axial tests

3.1.1. Compression

Typical compressive stress–strain curves using cube specimen geometry are shown for three loading directions (see Fig. 5). The curves display an initial peak stress followed by a plateau with slight apparent hardening. The final stage of the curve corresponds to material densification. The observed anisotropy effect of the compressive behaviour is rather small. This is consistent with other results published in the literature (see e.g. Refs. [8,30]). The plateau region shows minor oscillations which are typically associated with local failure of cell rows. The plateau region corresponds to the formation of localisation bands that multiply or propagate over the entire sample [6,7,32]. The fact that

Table 3

Experimental values for the initial (fracture/yield) stress measured in tension, compression, torsion and combined tension–compression/torsion tests

Tensile tests				Compression tests, cuboid specimens	Torsion tests, T2	Tension–compression/torsion tests, T2					
T1	T2	T3	T4			Non-proportional, axial stress (MPa)			Proportional, slope (deg)		
									45	135	
									–2	1	2
1.93	1.91	1.70	2.22	–2.16	1.48	0.55	1.2	0.55	1.15	1.29	
1.96	1.93	1.86	2.93	–2.41	1.68	0.94	1.42	0.82	1.35	1.45	
2.01	1.94	1.87	2.75	–2.53	1.73	0.98	1.53	1.17	1.49	1.68	
2.14	2.16	2.12	3.72	–2.59	1.87	1.28	1.82	1.35	1.6	1.78	
2.32	2.19	2.18	2.89	–2.68	1.92	1.66	1.92	1.65	1.7		
2.33	2.19	2.37	2.42	–2.89	2.08	1.68	2		1.9		
2.34	2.23	2.37	1.89	–2.92	2.2						
2.34	2.25	2.49	2.79								
2.35	2.26	2.50	2.22								
2.43	2.35	2.51	4.33								
2.48	2.38	2.5	2.77								
2.54	2.47	2.56	2.80								
2.54	2.48	2.58	2.84								
2.62	2.55	2.60	2.98								
2.63	2.56	2.64	2.99								
2.63	2.59	2.78	2.93								
2.68	2.69	2.80									
2.68	2.80	2.81									
2.76	3.03	2.82									
2.78	3.06	2.82									
2.80	3.06	2.94									
2.85	2.98										
2.87	3.22										
2.91	3.28										
3.01											
3.07											
3.12											

All values are given in MPa.

the deformation bands are associated with local brittle failure has been checked with an interrupted compressive test. After a compressive strain of 6%, the specimen is unloaded and loaded again in tension. It is found that the material does not oppose measurable resistance in tension any more. This is the reason why in this paper no distinction is made between “yielding” effects observed under predominantly compressive conditions and brittle fracture effects observed under predominantly tensile loading condition.

On the curves shown in Fig. 5, the stress is the force divided by the initial section, and the strain is the thickness variation of the specimen divided by the initial thickness. The denominations stress and strain do not take into account the heterogeneity of deformation of the specimen. The

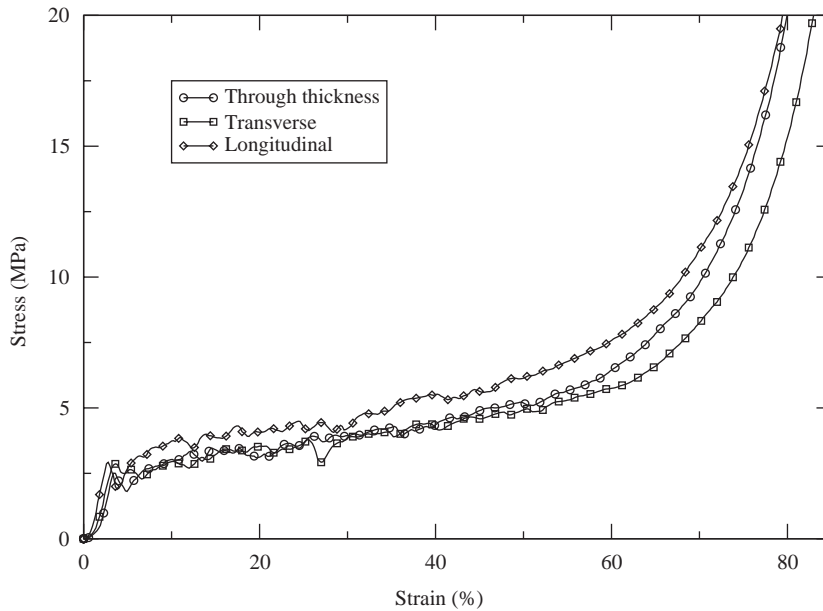


Fig. 5. Compression stress–strain curves (cube specimen geometry).

yield/fracture stress in compression is defined at the first peak observed on the stress–strain curves for the cube specimens compressed between two flat plates. The results of yield strength measured in compression are given in Table 3. These results give a mean yield strength of 2.6 MPa.

3.1.2. Tension

A typical tensile stress–strain curve is presented in Fig. 6. The initial horizontal tangent is associated with the alignment and the gap of the tensile apparatus. It is followed by a linear elastic regime. The final stage of the curve corresponds to brittle fracture. Fracture occurs generally far from the grips and the orientation of the fracture surface is perpendicular to the tensile axis. The fracture strength in tension was taken as the maximum stress sustained by the specimen. Fracture strengths in tension show a significant scatter which is reported in Table 4. The results are also plotted in Fig. 7. The average and dispersion are found to depend on the volume of the tested specimens: they decrease with increasing specimen size. The size effect is less significant on the mean fracture strength than on the standard deviation but does exist. The precision c of the estimation of mean fracture strength is given by $c = D_\sigma / \sqrt{n}$ where n is the number of samples tested for a given volume. It can be checked from Table 4 that this precision is sufficient to ensure that the mean fracture strength actually decreases from T4 to T1. For an increase of volume size by a factor of 4 the mean fracture strength is reduced by about 15% whereas the dispersion is almost divided by 2. It should also be noted that the mean tensile strength is close to the yield strength measured in compression.

Observations of the fracture surface show that brittle fracture initiates mainly around big cells. SiC particles are present along the crack path of the cell walls (Fig. 8, see also Ref. [27]).

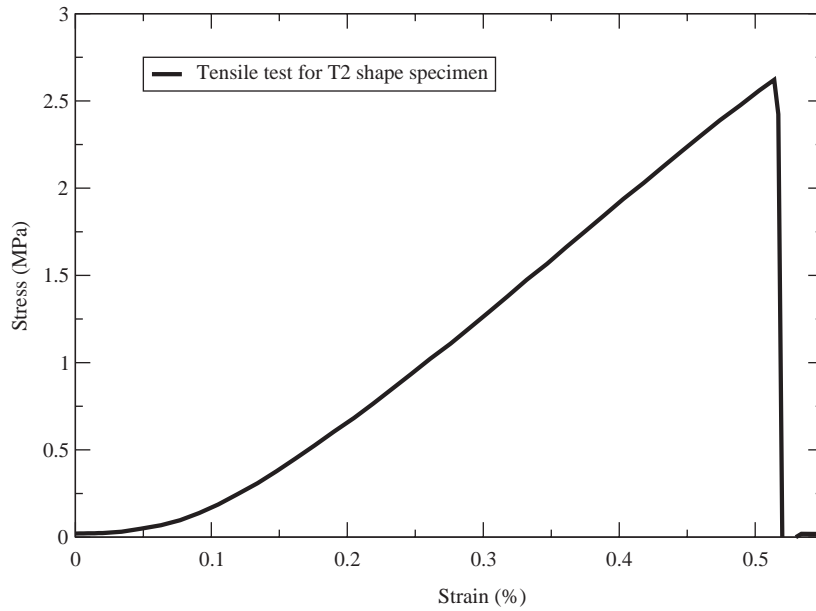


Fig. 6. Stress–strain curve of a tensile test on aluminium foam.

Table 4

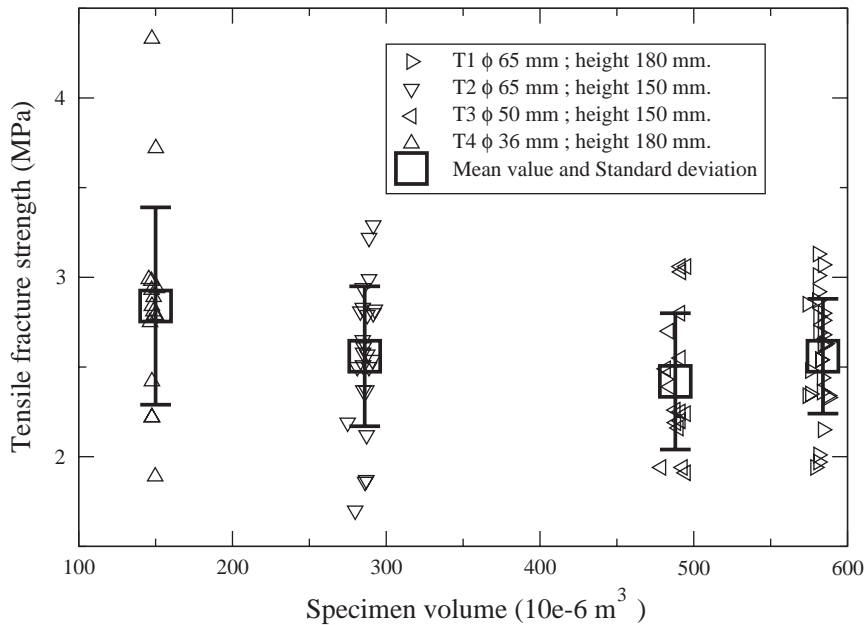
Experimental and predicted mean tensile strength and corresponding dispersion for all tensile tests

Specimen	Tensile tests			
	Mean stress (MPa)		Standard deviation (MPa)	
	Experimental	Weibull's prediction	Experimental	Weibull's prediction
T1	2.56	2.41	0.33	0.35
T2	2.43	2.47	0.35	0.36
T3	2.56	2.63	0.40	0.38
T4	2.84	2.85	0.57	0.41

3.1.3. Shear and torsion

A typical shear stress–strain curve is presented in Fig. 9 where a mainly brittle behaviour is observed. In these tests, a crack initiates in the core of the sample and propagates parallel to the load axis along one-third of the sample length and then deviates to the joint between the foam and the shear grips. Only four tests were carried out leading to the following values for the maximum shear stress: 1.7, 1.75, 1.9 and 2.0 MPa.

Typical torsion torque/angle curves are given in Fig. 10. The plotted shear stress is $2M/\pi R^3$ where M is the prescribed torque and R the radius of the specimen. The plotted shear strain is $\gamma = R\theta/L$ where L is the length of the specimen and θ is the measured angle. The plot shows a short elastic domain and then two regions of apparent hardening. The shear strength is defined as the limit of the



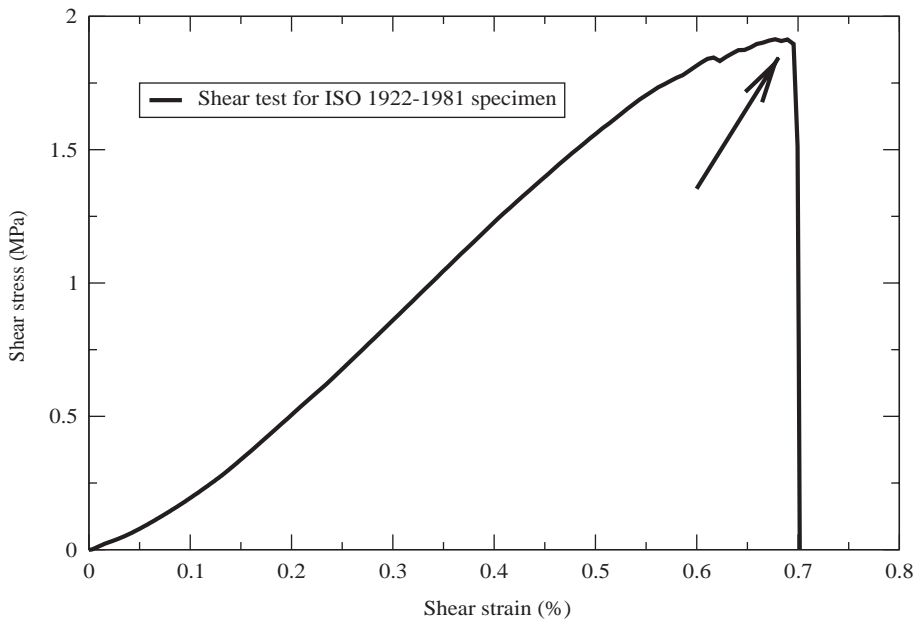


Fig. 9. Shear stress/strain curve for a shear test.

fails, a stress redistribution causes the stress to reach the failure level for neighbouring cell walls. This process is repeated until final fracture takes place. Cracks initiate at several sites but only one of them propagates to cause final failure. The two hardening stages are difficult to explain but may be associated with different cell size populations. The obtained mean value for the shear stress and the corresponding standard deviation are 1.85 and 0.24 MPa, respectively. Note that the shear strengths obtained for these torsion tests are consistent with those obtained for shear tests. The fracture surface is generally a spiral at an angle of about 45° with respect to the specimen axis (Fig. 10b).

3.2. Multi-axial tests

The results for the multi-axial tests are given in Tables 3 and 5. Typical tension/compression–torsion tests are presented in Figs. 11 and 12 in the case of non-proportional loading. In this case, the axial load is applied and maintained constant during subsequent torsion. Both cases of positive and negative axial forces have been tested. In these tests, the critical shear strength τ_0 is defined as in the torsion case. In Figs. 11 and 12, the position on the shear stress–strain curve where the critical shear stress was determined is also indicated by an arrow. The fracture surfaces of the samples are also shown in Figs. 11 and 12. For low positive values of the axial stress, the shape of the shear stress vs. torsion angle curve is similar to the torsion curve with the elastic phase followed by two hardening zones (Fig. 10). However, as the axial stress increases, the two hardening zones become less pronounced and the fracture surface becomes more and more horizontal as in the pure tension case.

For the proportional loading path, the axial force and torque are applied simultaneously and follow a straight line with a given slope in the torque/force space. The results show also a significant

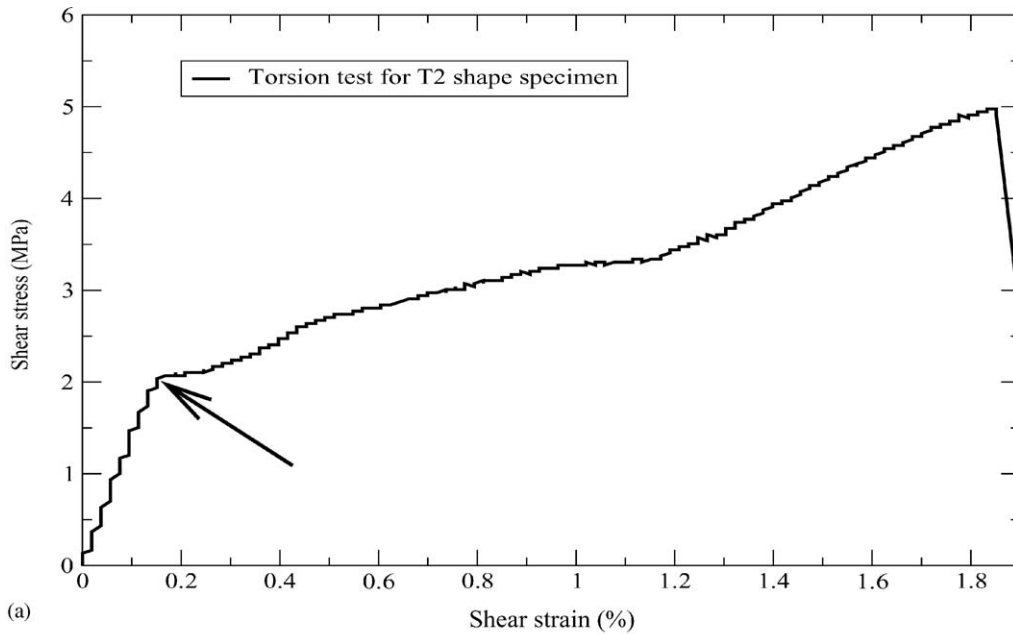


Fig. 10. (a) Stress–Strain curve for a specimen in torsion. (b) Corresponding fracture surface of the specimen (specimen diameter: 65 mm).

scatter but, for a given slope $\alpha = 45^\circ$ (tension–torsion) or $\alpha = 135^\circ$ (compression–torsion, see the definition of the angle α in Fig. 4), the mean fracture/yield stresses are comparable. At this stage, the comparison between the two different paths cannot be done without introducing an equivalent stress.

Table 5

Experimental and predicted mean yield effective stress and corresponding dispersion for non-proportional and proportional multi-axial loading conditions

Non-proportional loading				
Axial stress σ_0 (MPa)	Mean shear stress $\bar{\tau}_{0 \sigma_0}$ (MPa)		Shear stress standard deviation $D_{\tau \sigma_0}$ (MPa)	
	Experimental	Weibull's prediction	Experimental	Weibull's prediction
-2	1.18	1.19	0.44	0.51
0	1.85	1.85	0.24	0.27
1	1.65	1.71	0.31	0.30
2	1.11	1.19	0.43	0.51

Proportional loading				
α (deg)	Mean yield stress \bar{k} (MPa)		Yield stress standard deviation D_k (MPa)	
	Experimental	Weibull's prediction	Experimental	Weibull's prediction
45	1.53	1.51	0.26	0.22
135	-1.55	-1.51	0.22	0.22

4. Discussion and modelling

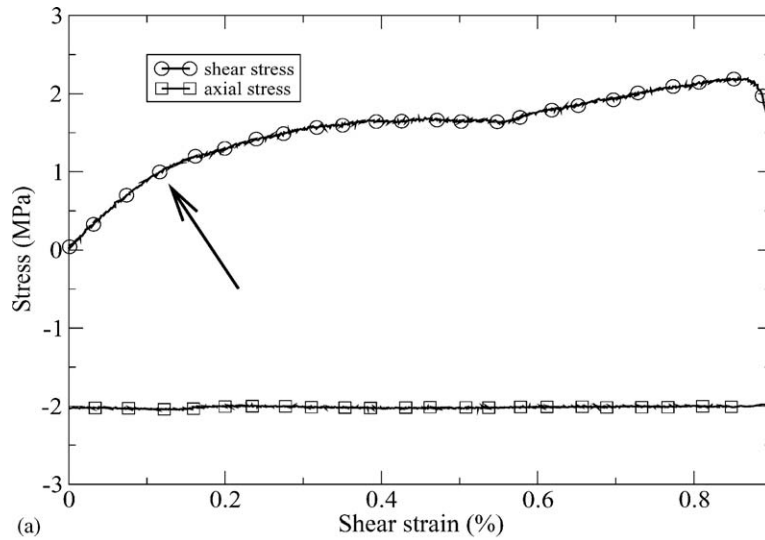
The discussion of the previous results is focused on the interpretation and modelling of the response of the aluminium foam under uni- and multi-axial loading. A model is introduced to account for the size effect and the scatter observed in test results. This model must be able to predict the mean response and the dispersion for each loading condition. Accordingly, a statistical model is developed in the first subsection to account for the size effect observed in tension tests. Then it is shown that the model can be extended to shear/torsion and multiaxial loading, thus providing an interpretation of the scatter observed for all loading conditions. Finally, a tentative micromechanical model taking into account brittle fracture of larger cells in foams is proposed.

4.1. Statistical analysis and size effect for uni-axial loading conditions

The fracture stress of the 88 tested tensile specimens are ranked in increasing stress order (see Table 3). The cumulative probability of failure for a given applied stress corresponding to the rank i can then be estimated as

$$P_{Ri} = \frac{i}{N + 1}, \tag{1}$$

where N is the total number of samples tested. Two laws of probability have been tested to describe the experimental results: normal and Weibull distributions. The best agreement concerning mean values and scatter was obtained with the Weibull distribution as shown in Fig. 13 for all volumes. The cumulative probability of failure at a tensile stress σ for a Weibull distribution is



(b)

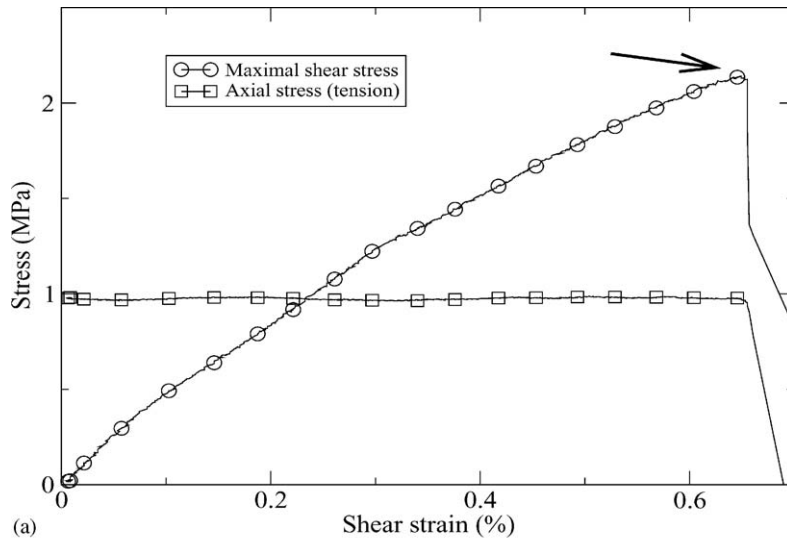
Fig. 11. (a) Stress–strain curve for a non-proportional compression–torsion test. (b) Corresponding fracture surface of the specimen (specimen diameter: 65 mm) after separation.

given by

$$P_R = 1 - \mathcal{F}(\sigma) = 1 - \exp \left[-\frac{V}{V_0} \left(\frac{\sigma}{\sigma_u} \right)^m \right], \quad (2)$$

where V is the volume of the sample, V_0 is a reference volume, σ_u is the scale factor and m is Weibull's modulus [24,26]. \mathcal{F} is the probability distribution function. The parameters σ_u and m were identified taking all tensile data into account, i.e. the results obtained for the four considered volumes. The reference volume V_0 , regarded as the typical size of a statistically representative volume element of material, was taken equal to 100 cm^3 . The values obtained for the Weibull parameters from the tensile tests are then

$$m = 8 \quad \text{and} \quad \sigma_u = 3.21 \text{ MPa}. \quad (3)$$



(b)

Fig. 12. (a) Stress–strain curve for a non-proportional tension–torsion test. (b) Corresponding fracture surface of the specimen (specimen diameter: 65 mm).

In Fig. 7, the experimental mean fracture stress seems to saturate at about 2.5 MPa. A threshold parameter could be introduced in Eq. (2) to represent this saturation effect. However, in the absence of tests on specimens with larger sizes no threshold parameter was introduced.

The value of the Weibull modulus is in the range of those found for engineering ceramics and far from that corresponding to dense metallic materials which are usually found to be of the order of 15–20 (see e.g. Ref. [26]). A value of $m = 10$ has been found by McCullough et al. in [5] for a powder-route aluminium foam. With these parameters, the predicted cumulative failure probabilities are plotted in Fig. 13 and compared to experimental results for the four specimen volumes. This comparison can also be made from the results reported in Table 4. In Fig. 13, it is observed that the experimental distributions are well described. It is worth noting that the same set of Weibull parameters is used to account for all tested volumes. Very often the parameters are identified for

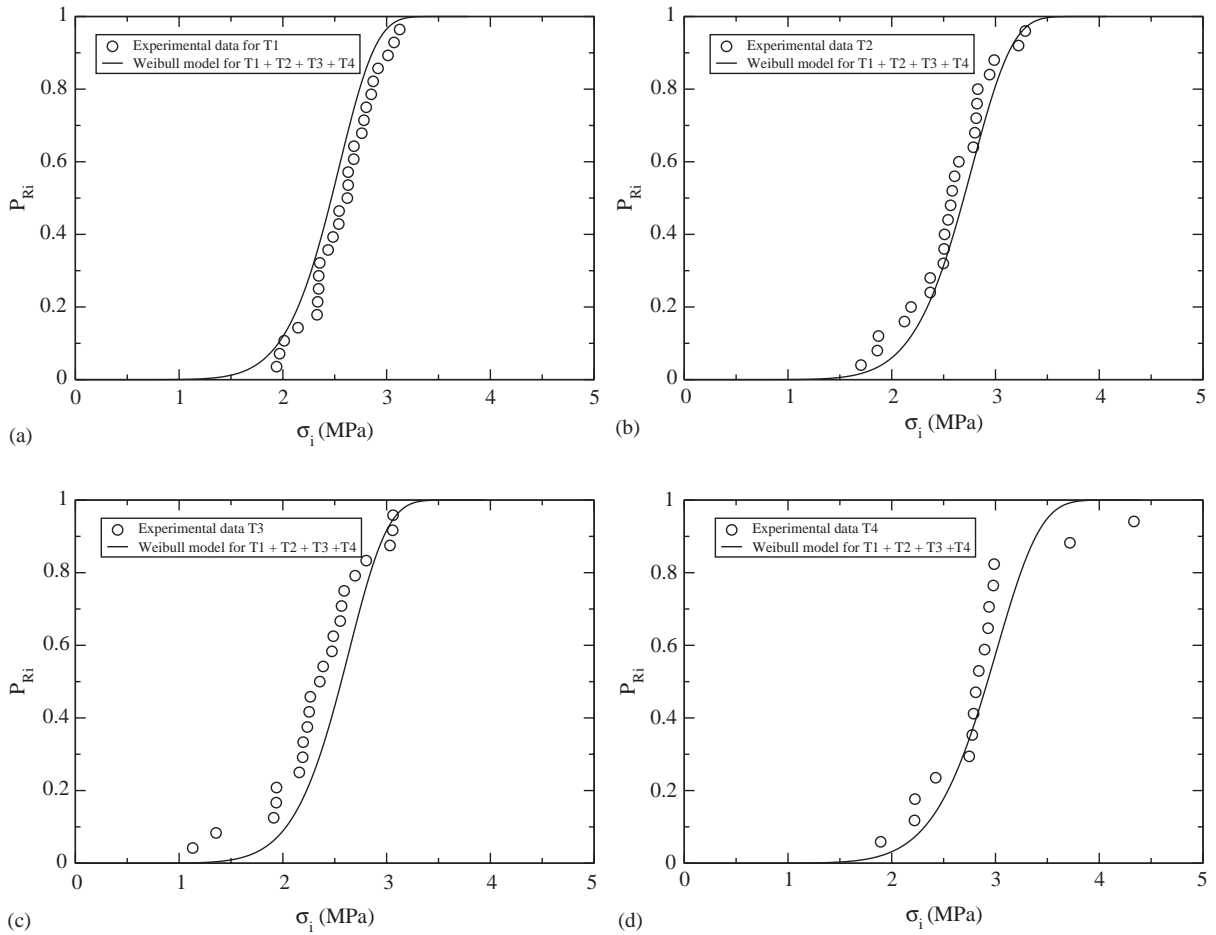


Fig. 13. Fracture probability distributions in tension for the specimen sizes T1–T4 (figures (a) to (d), respectively): experimental results and prediction according to Weibull's model.

a single volume, which is not sufficient to prove that Weibull's law is a well-suited model. Using Weibull analysis, the expected mean tensile stress $\bar{\sigma}$ and standard deviation D_{σ}^2 depend on the specimen size as follows:

$$\bar{\sigma} = \frac{\sigma_u}{(V/V_0)^{1/m}} \Gamma\left(\frac{m+1}{m}\right), \quad (4)$$

$$D_{\sigma}^2 = \frac{\sigma_u^2}{(V/V_0)^{2/m}} \left[\Gamma\left(\frac{m+2}{m}\right) - \Gamma^2\left(\frac{m+1}{m}\right) \right], \quad (5)$$

where Γ is the Gamma function. Table 4 displays for each specimen type the experimental and predicted mean stress and standard deviation. The size effect appears clearly since the dispersion and mean stress to fracture decrease when the specimen volume increases. This predicted behaviour is in good agreement with the results shown in Fig. 7. However, a weakness of the Weibull statistics

in the present case is that the ratio $\bar{\sigma}/D_\sigma$ according to Eqs. (4) and (5) does not depend on the volume, which is not really observed in the experiments. An improvement of the model concerning this point is not attempted in the present work since the agreement between experiment and model remains satisfactory.

In compression, the peak stress also displays a significant scatter and an attempt was made to apply the Weibull analysis to these compression results. For that purpose, the tensile stress in Eq. (2) is replaced by the absolute value of the peak stress. For the cube specimens, the mean first peak stress of the tested samples is equal to 2.6 MPa which is slightly higher than the mean tensile strength for equivalent volume sizes (597 cm³). The identification of a Weibull distribution for the compressive peak stress leads to the following values:

$$m = 8.9 \quad \text{and} \quad \sigma_u = 3.27 \text{ MPa.} \tag{6}$$

These values are close to those found for tensile loading. It shows that the failure statistics in tension and compression are not significantly different. In Ref. [5], McCullough et al. found $m = 12$ for a powder–route aluminium foam in compression. This strongly suggests that it is possible to use a unified statistical model valid for both tension and compression and also for other loading conditions.

4.2. Extension of the Weibull's analysis to torsion tests

The torsion tests also show a significant scatter (standard deviation 0.24 MPa). For fixed Weibull parameters identified from tensile loading, the aim is to check whether the model can be used to predict the dispersion for other types of loading. In this section, the case of torsion tests is investigated. The first step is to decide which stress should be used in Eq. (2) in the case of torsion test. An invariant effective stress function $\hat{\sigma}$ has to be defined. This effective stress should coincide with the absolute value of axial stress component in tension and compression. Rankine's criterion (maximum normal stress criterion) is a good candidate. However, this criterion is not suitable since it predicts that the yield stress for torsion test must be equal to the tensile yield stress, which is not the situation observed here. The mean yield strength in torsion and shear is 1.85 MPa instead of 2.43 MPa in tension. A von Mises equivalent stress can also be considered. This criterion sets the yield shear stress τ_0 to $\sigma_0/\sqrt{3} = 1.42$ MPa, which is too low compared to the mean experimental value. Several authors have shown that an elliptical yield function involving both the stress deviator and the trace of the stress tensor, can be used to describe the mechanical behaviour of metal and polymer foams for several types of load ranging from axial compression to hydrostatic compression [3,7,11,12,21]. The effective stress $\hat{\sigma}$ is then defined as

$$\hat{\sigma} = \sqrt{\frac{3}{2} C \underline{\underline{s}} : \underline{\underline{s}} + F(\text{Trace } \underline{\underline{\sigma}})^2}, \tag{7}$$

where $\underline{\underline{s}}$ is the deviatoric part of the stress tensor $\underline{\underline{\sigma}}$. C and F are material parameters that may depend on the current porosity. In tension and compression, this effective stress is equal to $\sqrt{C + F}|\sigma|$ where σ is the uni-axial stress component. Accordingly, the effective stress coincides with σ in tension if

$$C + F = 1. \tag{8}$$

This relation is assumed to hold in the sequel. This allows Eq. (2) to be re-written as

$$P_R = 1 - \mathcal{F}(\hat{\sigma}) = 1 - \exp \left[-\frac{V}{V_0} \left(\frac{\hat{\sigma}}{\sigma_u} \right)^m \right]. \tag{9}$$

Another difficulty arises in the case of torsion tests performed on solid bars, since the stress field is not uniform over the sample section. The stress field $\tau(r)$ is linear in the elastic regime, maximal at the circumference and zero at the center of the section:

$$\tau(r) = \frac{\tau_0}{R} r, \quad (10)$$

where R is the radius of the specimen and τ_0 is the maximum value of shear stress at the circumference. As the stress is not uniform through the sample volume, an integral form of Weibull's repartition function has to be used in the fracture probability distribution [25,33]

$$\mathcal{F}(\hat{\sigma}) = \exp \left[- \int_V \left(\frac{\hat{\sigma}}{\sigma_u} \right)^m \frac{dV}{V_0} \right] = \exp \left[- \int_V \left(\frac{\sqrt{3C}\tau(r)}{\sigma_u} \right)^m \frac{dV}{V_0} \right]. \quad (11)$$

The mean shear stress is then computed as

$$\bar{\tau} = \frac{\sigma_u}{\sqrt{3C}((2/(m+2))(V/V_0))^{1/m}} \Gamma \left(\frac{m+1}{m} \right). \quad (12)$$

In Eq. (12), the coefficient C can be identified from the experimental value of the mean shear strength keeping the Weibull parameters identified in the tension case. The shear strength of a torsion test is taken as the maximum stress τ_0 at the outer surface in the elastic regime. The obtained mean value is 1.85 MPa. This experimental mean shear strength is directly used to identify the parameter C . Then Eq. (8) gives the parameter F . Parameter identification gives $C = 0.89$ and $F = 0.11$. In Ref. [11], Deshpande and Fleck found $C = 0.7$ and $F = 0.3$ for their elliptical yield surface but in the case of axisymmetric compression. After the identification, as for the tension case, the prediction capability of the model can be tested by computing the expected variance of the results

$$D_{\bar{\tau}}^2 = \frac{\sigma_u^2}{3C((2/(m+2))(V/V_0))^{2/m}} \left[\Gamma \left(\frac{m+2}{m} \right) - \Gamma^2 \left(\frac{m+1}{m} \right) \right]. \quad (13)$$

The prediction is 0.27 MPa. It is in good agreement with the experimental scatter of 0.24 MPa. This confirms the ability of the model to account simultaneously for tension, compression and torsion tests.

4.3. Extension of the statistical analysis to multi-axial loading conditions

The applicability of the above statistical model characterised by a Weibull probability distribution and the introduction of the effective stress $\hat{\sigma}$ is now assessed in the more complex case of multi-axial loading. The Weibull parameters are still unchanged (see Eq. (3)) and the coefficients C and F keep the values found in the previous section. Both types of multi-axial stress paths 1 and 2 shown in Fig. 4 are analysed.

4.3.1. Non-proportional loading conditions

In the experimental procedure, the tension/torsion test is carried out by applying the axial stress first, under axial load control, followed by the shear stress using the rotation angle control mode. Thus, for a given axial stress σ_0 applied during the first part of the test, the aim is to predict the mean shear stress and standard deviation using the statistical model. Note that the specimen can break during the loading along the tension path. In this case, these weakest specimens cannot be used in

the analysis. This means that a conditional probability must be considered: it is the probability that the specimen breaks for a shear component τ_0 provided that it was able to sustain the pre-load σ_0 . The probability distribution takes now the form

$$\mathcal{F}_{|\sigma_0}(\tau_0) = \exp \left[- \int_V \left(\frac{\hat{\sigma}}{\sigma_u} \right)^m \frac{dV}{V_0} \right] = \exp \left[- \int_V \left(\frac{\sqrt{3C(\tau_0 r/R)^2 + F\sigma_0^2}}{\sigma_u} \right)^m \frac{dV}{V_0} \right]. \quad (14)$$

The density of conditional probability for a fixed prescribed axial component σ_0 is then given by the partial derivative with respect to τ_0 :

$$f_{|\sigma_0}(\tau_0) = \frac{\partial}{\partial \tau_0} [\mathcal{F}_{|\sigma_0}(\tau_0)]. \quad (15)$$

Thus, for a fixed amount of axial stress σ_0 , the mean shear stress $\bar{\tau}$ is given by

$$\bar{\tau}_{|\sigma_0} = \int_0^\infty \tau_0 f_{|\sigma_0}(\tau_0) d\tau_0. \quad (16)$$

The corresponding shear stress standard deviation is given by

$$D_{\tau|\sigma_0}^2 = \int_0^\infty \tau_0^2 f_{|\sigma_0}(\tau_0) d\tau_0 - \left[\int_0^\infty \tau_0 f_{|\sigma_0}(\tau_0) d\tau_0 \right]^2. \quad (17)$$

The values of $\bar{\tau}_{|\sigma_0}$ and $D_{\tau|\sigma_0}^2$ are computed numerically since no closed-form expression could be worked out. Table 5 gives the mean shear stress and the shear stress standard deviation for several values of prescribed axial stress. The predicted curve of mean shear strength and the corresponding intervals of confidence are shown in Fig. 14. It is interesting to note that this curve is not elliptical but is rather bell-shaped. This is due to the fact that it represents a conditional probability distribution for the specific considered non-proportional loading path. For the given example of a tensile loading of 2 MPa, which is around the mean yield strength in tension, several specimens broke during the first phase of loading. Thus, the first part of the loading path acts as a filter on the quality of the specimen. After this first loading phase, two extreme cases can be encountered. The first one is the case of specimens which were about to fail during the tensile loading and then will not oppose a great resistance to torsion. The second one is the case of specimens that were also able to pass through the first tensile loading phase but are among those with low defect density and then will be able to oppose a great resistance to torsion. This filtering effect on the quality of the specimens explains the evolution of the mean standard deviation vs. the axial stress and in particular the existence of the largest dispersion when the applied axial stress is close to the mean axial strength. It can be noticed that a very good agreement is reached between experiment and modelling in the tension/torsion domain as well as in the compression/torsion one.

4.3.2. Proportional loading conditions

It is also possible to calculate the mean stress and the standard dispersion along a proportional loading path. This path is described by

$$\sigma = k \cos \alpha,$$

$$\tau = k \sin \alpha,$$

$$\hat{\sigma} = k \sqrt{3C \sin^2 \alpha + \cos^2 \alpha}, \quad (18)$$

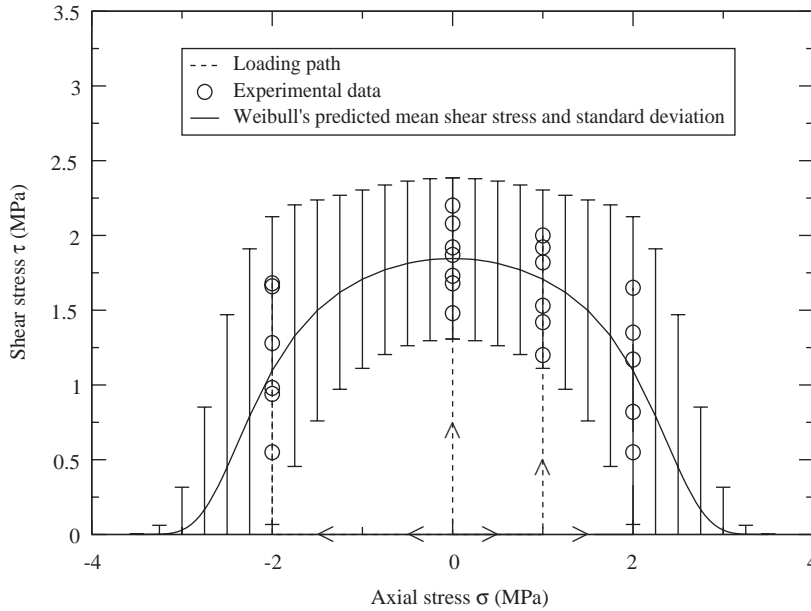


Fig. 14. Statistical yield criterion for non-proportional loading path 1: axial tension followed by torsion. Mean yield shear stress for prescribed axial stress and corresponding interval of confidence.

where α is an angle characterising the linear loading path in the (σ, τ) plane, and k varies from 0 to the fracture stress. The probability distribution takes then the form

$$\begin{aligned} \mathcal{F}(k) &= \exp \left[- \int_V \left(\frac{\sqrt{3C\tau^2 + \sigma^2}}{\sigma_u} \right)^m \frac{dV}{V_0} \right] \\ &= \exp \left[- \frac{V}{V_0 \sigma_u^m 3C(m/2 + 1) \sin^2 \alpha} k^m ((3C \sin^2 \alpha + \cos^2 \alpha)^{m/2+1} - (\sin \alpha)^{m+2}) \right]. \end{aligned} \tag{19}$$

Note that F does not appear in Eqs. (18) and (19) because Eq. (8) has been taken into account. The probability density becomes

$$f(k) = \frac{d}{dk} [\mathcal{F}(k)]. \tag{20}$$

For a proportional loading test, the mean effective stress is given by the mean value of k :

$$\bar{k} = \int_0^\infty k f(k) dk \tag{21}$$

$$\bar{k} = \frac{\sigma_u}{(V/V_0)^{1/m}} \left(\frac{3C(m/2 + 1) \sin^2 \alpha}{(3C \sin^2 \alpha + \cos^2 \alpha)^{m/2+1} - (\cos \alpha)^{m+2}} \right)^{1/m} \Gamma \left(\frac{m + 1}{m} \right). \tag{22}$$

The corresponding standard deviation is calculated as

$$D_k^2 = \int_0^\infty \tau_0^2 f(k) dk - \left[\int_0^\infty k f(k) dk \right]^2, \tag{23}$$

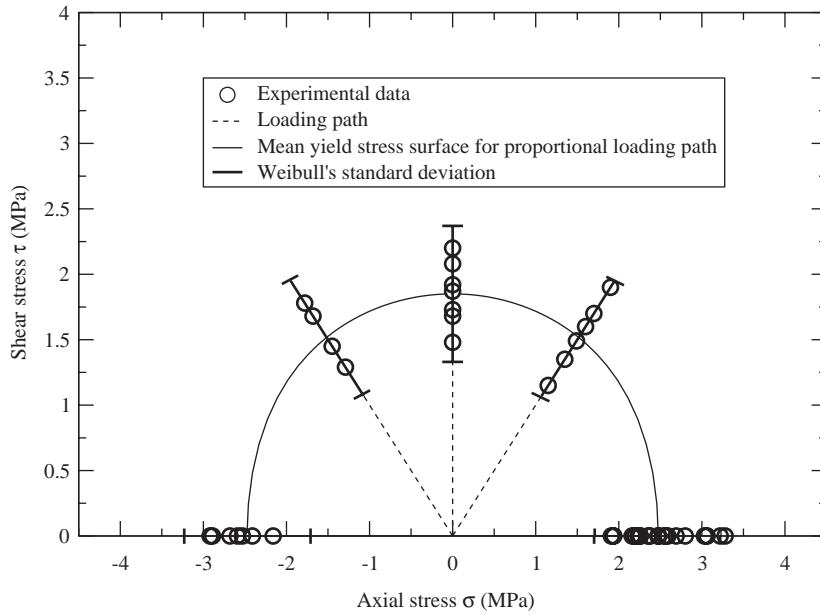


Fig. 15. Statistical yield criterion for proportional loading path. Experimental data vs. model prediction.

$$D_k^2 = \frac{\sigma_u^2}{(V/V_0)^{2/m}} \left(\frac{3C(m/2 + 1) \sin^2 \alpha}{(3C \sin^2 \alpha + \cos^2 \alpha)^{m/2+1} - (\cos \alpha)^{m+2}} \right)^{2/m} \times \left[\Gamma \left(\frac{m+2}{m} \right) - \Gamma^2 \left(\frac{m+1}{m} \right) \right]. \quad (24)$$

It can be checked that for $\alpha = 90^\circ$ or 0° the mean stress and standard deviation for a torsion test or tensile test, respectively, are retrieved. Here, there is no conditional probability since the shear and axial stresses are applied simultaneously. Fig. 15 gives the curve corresponding to the mean yield effective stress in (σ, τ) space. This curve shows a quasi-elliptical shape. The experimental results in two directions ($\alpha = -45^\circ, 45^\circ$) are compared with the obtained predictions in Fig. 15 and in Table 5. A good agreement is obtained for both mean value and variance. It is worth emphasising that these results are pure predictions of the model since the parameters have been identified in tension and torsion only.

4.4. A tentative micromechanical model

The Weibull statistics used in this work corresponds to a weakest link model in which the fracture/yield of one defect leads to the fracture/yield of the whole stressed volume. In Ref. [26], a similar assumption was made to interpret brittle fracture in a ferritic steel. In this material, it was assumed that fracture was initiated from preexisting cleavage cracks. The Weibull distribution was derived analytically from the statistics of distribution of cleavage crack lengths combined with linear fracture mechanics concepts. What are the corresponding defects in aluminium foams and can the

Weibull statistics be derived? In Refs. [18,34] Huang and Gibson consider for an open-cell foam that the failure in bending of a cell strut made of brittle material is the weakest link. They applied the Weibull's theory to this strut in bending and found a dependence of the fracture toughness of the foam on the cell size and the Weibull modulus of the cell wall material. Here, a different point of view is adopted. It is postulated that the defects are the largest cells in the heterogeneous distribution of cell sizes. A simple model is then proposed based on Gibson and Ashby's cell model for foam [3] and the knowledge of the statistical distribution of cell size.

For an open-cell brittle foam, Gibson and Ashby [3] have shown that a cell edge will fail when the moment acting on it exceeds

$$M_f = \frac{1}{6} \sigma_w t^3, \quad (25)$$

where σ_w is the fracture stress of the cell edge material and t is the thickness of the edge, assumed to be identical for all cell sizes. The corresponding fracture stress of the foam can then be evaluated as in Ref. [3]:

$$\sigma \propto \frac{M_f}{l^3}, \quad (26)$$

where l is the edge length. This equation combined with Eq. (25) can also be used to compute the smallest critical cell size l_c responsible for fracture of the foam at stress σ

$$l_c \propto t \left(\frac{\sigma_w}{\sigma} \right)^{1/3}. \quad (27)$$

The probability of finding a cell of a given size is a function of the volume of material involved. It is assumed that the stressed volume can be divided in smaller volumes V_0 . V_0 must be large enough for the probability of finding a cell of sufficient size not to be vanishingly small. Statistical independence of neighbouring volumes V_0 is also assumed. Thus, V_0 must include a sufficient number of cells. In each volume V_0 , the probability of finding a cell of edge length between l and $l + dl$ is taken as

$$p(l) dl = \frac{\alpha}{l^\beta} dl, \quad (28)$$

where a simple power law is assumed for the probability distribution. α and β are material parameters once V_0 is known. Thus, in a given volume V_0 , where the stress level is σ , the probability of failure is

$$p(\sigma) = \int_{l_c}^{\infty} p(l) dl, \quad (29)$$

where the critical length l_c is given by Eq. (27). It follows that

$$p(\sigma) \propto \frac{\alpha}{1-\beta} \left(\frac{\sigma_w t}{6} \right)^{(1-\beta)/3} \sigma_c^{(\beta-1)/3} = \left(\frac{\sigma_c}{\sigma_u} \right)^m \quad (30)$$

with $m = (\beta - 1)/3$ and σ_u depends on t, α, β and σ_w .

In the case of closed-cell foams, membrane stresses can be predominant and as in Ref. [3], Eq. (27) should be replaced by

$$l_c \propto t \left(\frac{\sigma_w}{\sigma} \right)^{1/2}. \quad (31)$$

This leads to a different value of the Weibull modulus

$$m = \frac{\beta - 1}{2}. \quad (32)$$

Each volume $V_i = V_0$ among the N ones paving the entire specimen volume V is subjected to the stress state σ_i . The cumulative probability of failure for the entire specimen is then

$$P_R = 1 - \prod_{i=1}^N (1 - p(\sigma_i)). \quad (33)$$

For small enough probabilities $p(\sigma_i)$, one obtains

$$\ln(1 - P_R) = -\sum_{i=1}^N p(\sigma_i) \simeq -\frac{V}{V_0} \left(\frac{\sigma}{\sigma_u} \right)^m \quad (34)$$

if σ is almost constant in the sample. For a varying stress field, the last term can be replaced by $\int_V p(\sigma) dV/V_0$. As a result, the material is shown to follow the Weibull's statistics [26] and the distributions used in this work are retrieved (Eqs. (2) and (11)).

Image analysis of several sections of an aluminium foam sample from optical microscopy and X-ray tomography provides the distribution of cell sizes [28]. The power law model in Eq. (28) for cell size distribution is calibrated on the last part of the distribution concerning large sizes only. The found parameter β is close to 5. This leads to a Weibull modulus of $m=1.7$ for open-cell foams and $m=2$ for closed-cell foams. This values are much smaller than the parameter m close to 8 found in this work. This indicates that a micromechanical model taking only brittle failure into account underestimates the actual Weibull modulus for metallic foams. A more realistic model should include the plastic yielding of the cell walls in addition to the subsequent brittle response as described in Ref. [8]. The model proposed in this subsection is clearly better-suited for purely brittle foams (see Ref. [3]). For instance, overall values of Weibull modulus for ceramic foams range from 1.5 to 6 [18,35,36].

5. Conclusions

Five main conclusions are drawn from this work:

- (1) A size effect has been evidenced in tension for four different cylindrical specimen sizes: the mean failure stress and the dispersion decrease with increasing volume. A classical Weibull model is able to account for both effects with a Weibull modulus close to $m=8$. This statistics is found to hold also for the first peak stress in compression. This brittle behaviour is related to the presence of several brittle phases in the aluminium alloy.
- (2) A model of statistical yield/failure surface is proposed based on the use of an effective stress. The effective stress is an elliptical combination of first and second invariants of the stress tensor. The model can predict the mean initial yield/failure stress and its expected dispersion for multi-axial loading conditions. The existence of such a unified model for various loading conditions is mainly due to the fact that the fracture mechanisms dominate with respect to plastic deformation processes.

- (3) The additional parameter entering the definition of the effective stress measure has been identified from the measured mean shear strength. The model predicts accurately the scatter in the observed shear strength. Good accordance between homogeneous shear tests and torsion tests is found regarding the initial yield/failure strength. Note however, that the shear test is associated with pure brittle behaviour of the foam. In torsion, two hardening regimes are observed. In the case of torsion, the stress field is not homogeneous and elementary volumes of size V_0 inside the tested sample are not subjected to a homogeneous stress but rather to a stress gradient. The yield shear stress was taken as the maximum stress evaluated at the outer surface. Again, the Weibull analysis is found to work well.
- (4) The statistical yield/fracture surface is validated along complex proportional and non-proportional multi-axial tests. A bell-shaped mean yield/fracture strength curve is found in the case of torsion with constant applied axial stress. A quasi-elliptical surface is found in the case of proportional tension/compression–torsion loading. Good agreement is observed between the mean and dispersion obtained experimentally and the predicted values. Note that the experimental results confirm the symmetry of the yield/fracture surfaces vs. tension/compression. This has been noticed previously for other loading conditions by Deshpande and Fleck [11,12].
- (5) The Weibull statistics has been derived from a statistical power-law distribution of cell sizes assuming deterministic brittle failure of cell struts or walls in closed or open-cell foams, as an extension of Beremin's model [26]. The model, mainly applicable to ceramic foams, underestimates the Weibull modulus of the investigated aluminium foam, which confirms that local brittle failure as well as plastic yielding are two competing deformation mechanisms.

The combined tension–compression/torsion tests have shown how the response of the material evolves from the well-known compression curve with a plateau, through the torsion curves with two hardening regimes, up to the brittle failure tensile curves. In compression, deformation takes place mainly in horizontal bands. The fracture surface of tensile specimens is also perpendicular to the sample axis. In torsion, typical spiral fracture surfaces are observed. Photographs provided in this work show the transitions between these extreme cases. It can be noted that the orientation of the fracture surfaces is compatible with a maximum normal stress criterion. However, such a criterion does not work to predict the fracture stress level. This suggests that a non-associated failure criterion may be necessary to predict both strength level and fracture surface orientation. The present work only provides an answer to the first point.

Currently, deterministic compressible plasticity models involving the effective stress used in this work are the main ingredient of finite element simulations of structural components [37]. The computation of structures containing aluminium foams using such a statistical multi-axial model is the next step for a reliable assessment of component behaviour.

Acknowledgements

The authors would like to thank Mr. D. Gordine from CGES-Ecole des Mines de Paris for machining of specimens and Mr. H. Benouali and Pr. L. Froyen (KU Leuven) for providing some results of X-ray tomography and image analysis. The authors also thank Hydro Aluminium for providing the aluminium foam.

References

- [1] Ma L, Zhenlun S. Cellular structure control of aluminium foam during foaming process of aluminium melt. *Scripta Materialia* 1998;39(11):1523–8.
- [2] Simone AE, Gibson LJ. Aluminium foams produced by liquid state processes. *Acta Materialia* 1998;46(10):3109–23.
- [3] Gibson LJ, Ashby MF. *Cellular solids*, 2nd ed. Cambridge: Cambridge University press; 1997.
- [4] Ashby MF, Evans A, Fleck NA, Gibson LJ, Hutchinson JW, Wadley HNG. *Metal foam: a design guide*. London: Butterworth, Heinemann; 2000.
- [5] McCullough KYG, Fleck NA, Ashby MF. Uniaxial stress–strain behaviour of aluminium alloy foams. *Acta Materialia* 1999;47(8):2323–30.
- [6] Bart-Smith H, Bastawros AF, Mumm DR, Evans AG, Sypeck DJ, Wadley HNG. Compressive deformation and yielding mechanisms in cellular Al alloys determined using X-ray tomography and surface strain mapping. *Acta Materialia* 1998;46:3583–92.
- [7] Chastel Y, Hudry E, Forest S, Petour-Chansac C. Mechanical behaviour of aluminium foams for various deformation paths: experiments and modelling. In: Banhart NFJ, Ashby MF, editors. *Metal foam and porous metal structures*. Berlin: Verlag MIT Publishing; 1999. pp. 263–8.
- [8] Andrews E, Sanders W, Gibson LJ. Compressive and tensile behaviour of aluminum foams. *Material Science and Engineering A* 1999;270:113–24.
- [9] Triantafillou TC, Zhang J, Shercliff TL, Gibson LJ, Ashby MF. Failure surfaces for cellular materials under multiaxial loads. II: comparison of models with experiments. *International Journal of Mechanical Sciences* 1989;31:665–78.
- [10] Gioux G, McCormack TM, Gibson LJ. Failure of aluminium foams under multiaxial loads. *International Journal of Mechanical Sciences* 2000;42:1097–117.
- [11] Deshpande V, Fleck N. Isotropic constitutive models for metallic foams. *Journal of Mechanics and Physics of Solids* 2000;48:1253–83.
- [12] Deshpande V, Fleck N. Multi-axial yield behaviour of polymer foams. *Acta Materialia* 2001;49:1859–66.
- [13] Chen C, Fleck N, Lu T. The mode I crack growth resistance of metallic foams. *Journal of Mechanics and Physics of Solids* 2001;49:231–59.
- [14] Silva MJ, Hayes WC, Gibson LJ. The effect of non periodic microstructure on the elastic properties of two dimensional cellular solids. *International Journal of Mechanical Sciences* 1995;37:1161–77.
- [15] Andrews E, Gioux G, Onck P, Gibson L. Size effects in ductile cellular solids. part II: experimental results. *International Journal of Mechanical Sciences* 2001;43:701–13.
- [16] Andrews E, Gibson L. The influence of cracks, notches and holes on the tensile strength of cellular solids. *Acta Materialia* 2001;49:2975–9.
- [17] Onck PR. Application of a continuum constitutive model to metallic foam DEN-specimens in compression. *International Journal of Mechanical Sciences* 2001;43:2947–59.
- [18] Huang JS, Gibson LJ. Fracture toughness of brittle foams. *Acta Metallurgica and Materiala* 1991;39(7):1627–36.
- [19] Gibson LJ, Ashby MF, Zhang J, Triantafillou TC. Failure surfaces for cellular materials under multiaxial loads. I: modelling. *International Journal of Mechanical Sciences* 1989;31:635–64.
- [20] Miller A. A continuum plasticity model for the constitutive and indentation behaviour of foamed metals. *International Journal of Mechanical Sciences* 2000;42:729–54.
- [21] Badiche X, Forest S, Guibert T, Bienvenu Y, Bartout J-D, Ienny P, Croset M, Bernet H. Mechanical properties and non-homogeneous deformation of open-cell nickel foams: application of the mechanics of cellular solids and of porous materials. *Materials Science and Engineering A* 2000;A289:276–88.
- [22] Hanssen AG, Hopperstad OS, Langseth M, Ilstad H. Validation of constitutive models applicable to aluminium foams. *International Journal of Mechanical Sciences* 2002;44:359–406.
- [23] Besson J, Abouaf M. Microstructural changes in alumina during HIP. *Material Science and Engineering A* 1989;109:37–43.
- [24] Weibull W. A statistical distribution function of wide applicability. *Journal of Applied Mechanics* 1951;9:293–7.
- [25] Evans AG, Jones RL. Evaluation of a fundamental approach for the statistical analysis of fracture. *Journal of American Ceramic Society* 1978;61:156–60.

- [26] Beremin FM. A local criterion for cleavage fracture of a nuclear pressure vessel steel. *Metallurgical and Materials Transactions A* 1983;14:2277–87.
- [27] Markaki AE, Clyne TW. The effect of cell wall microstructure on the deformation and fracture of aluminium-based foams. *Acta Materialia* 2001;49:1677–86.
- [28] Benouali A-H, Froyen L. On the mechanical and microstructural characterisation of aluminium foams. In: Banhart NAFJ, Ashby MF, editors. *Cellular metals and metal foaming technology*. Berlin: Verlag MIT Publishing; 2001. pp. 269–72.
- [29] Elmoutaouakkail A, Salvo L, Maire E, Peix G. 2D and 3D characterisation of metal foams using X-ray tomography. In: Banhart NAFJ, Ashby MF, editors. *Cellular metals and metal foaming technology*. Berlin: Verlag MIT Publishing; 2001. pp. 245–50.
- [30] Beals JT, Thompson MS. Density gradient effects on aluminium foam compression behaviour. *Journal of Materials Science* 1997;47(13):3595–600.
- [31] Sugimura Y, Meyer J, He M, Bart-Smith H, Grenestedt J, Evans A. On the mechanical performance of closed cell Al alloy foams. *Acta Materialia* 1997;45(12):5245–59.
- [32] Bastawros AF, Bart-Smith H, Evans AG. Experimental analysis of deformation mechanisms in a closed-cell aluminum alloy foam. *Journal of the Mechanics and Physics of Solids* 2000;48:301–22.
- [33] Lamon J, Evans A. Statistical analysis of bending strengths for brittle solids. *Journal of American Ceramic Society* 1983;66:177–82.
- [34] Huang JS, Gibson LJ. Fracture toughness of brittle honeycombs. *Acta Metallurgica and Materialia* 1991;39(7):1617–26.
- [35] Tuliani J-M, Montanaro L, Bell TJ, Swain MV. Semiclosed-cell mullite foams: preparation and macro and micromechanical characterization. *Journal of the American Ceramic Society* 1999;82(4):961–8.
- [36] Colombo P, Heilmann JR, Shelleman EL. Mechanical properties of silicon oxycarbide ceramic foam. *Journal of the American Ceramic Society* 2001;84(10):2245–51.
- [37] Blazy J-S. Comportement mécanique des mousses d'aluminium: caractérisations expérimentales sous sollicitations complexes et simulations numériques dans le cadre de l'élasto-plasticité compressible. PhD, Ecole des Mines de Paris, 2003.